An Impedance-Controlled Testbed for Simulating Variations in the Mechanical Fit of Wearable Devices

Alexander B. Ambrose, *Student Member, IEEE,* Chelse VanAtter, and Frank L. Hammond III, *Member, IEEE*

***Abstract*— The fit of a wearable device, such as a prosthesis, can be quantitatively characterized by the mechanical coupling at the user-device interface. It is thought that the mechanical impedance, specifically the stiffness and damping, of wearable device interfaces can significantly impact human performance while using them. To test this theory, we develop a forearm-mounted testbed with a motorized, two degree of freedom (2-DOF) gimbal to simulate variations in the mechanical fit of an upper-extremity wearable device during pointing and target tracking tasks. The two gimbal motors are impedance-controlled to vary the mechanical stiffness and damping between the user and the device's laser pointer end-effector. In this paper, experiments are conducted to determine the torque constants of the motors before implementation in the testbed, and to validate the accuracy of the joint impedance controller. The completed impedance-controlled wearable interface testbed is validated further by comparing the gimbal joint displacements and torques, recorded during 2-DOF base excitation experiments, to MATLAB Simulink simulation data.**

***Index Terms*— wearable robot, compliance and impedance control, human performance augmentation**

I. Introduction

Wearable devices are not rigidly attached to their users and, therefore, can modify the kinematics and kinetics of the wearers [1], [2]. Non-osseointegrated prostheses interfaces are typically custom-made for users to fit their unique limb anatomy, while other wearables intended to fit multiple users typically have some mechanism for adjusting the fit. This fit is difficult to tune quantitatively and is typically adjusted depending on user preferences determined from surveys like the QUEST and OPUS surveys [3], [4]. However, prosthesis fit has been shown to impact safety, usability, and user satisfaction [**?**], [5]. Mechanically, the fit of a prosthesis is thought to affect the impedance of the human-socket interface [6]. Impedance, in this mechanical sense, relates the forces and torques imparted on a system to its prismatic and rotational displacements. It is thought that the quality of fit, or specifically, the impedance at the human-socket interface not only affects wearable device comfort but also affects users' task performance and cognitive workload. This hypothesis is inspired by the fact that animals change the impedance of their joints to optimally perform tasks. For instance, during walking, humans control the impedance of their lower limbs depending on which phase of the gait cycle they are in to achieve a specific goal, such as minimizing metabolic cost or maintaining specific speeds [7], [8].

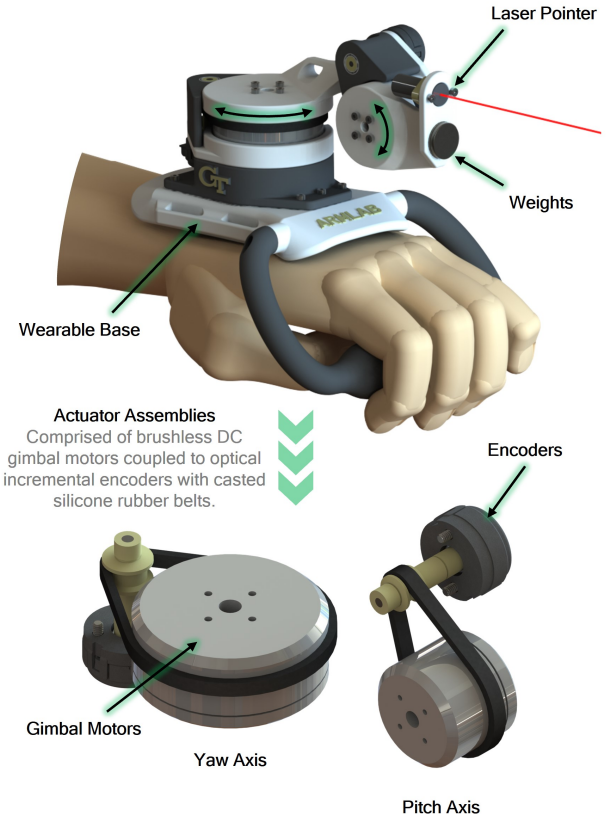

Fig. 1. Rendering of the wearable mechanical interface testbed. Two gimbal motors are used to control the impedance between the user and the laser pointer end-effector for simulating the level of fit of a wearable device in 2-DOF target tracking tasks.

Similar to how animals manipulate the impedance of their joints to suit certain activities, passive wearables also utilize specific impedance to improve human performance or comfort. For example, shoes are designed to have certain impedances depending on the tasks they are intended for [9]. Hiking boots are typically more rigid while running shoes may be more compliant [10], [11]. Passive prostheses are typically designed to mimic the impedance of the missing limb for a specific task such as walking or stair climbing [12]. Passive exoskeletons also take advantage of various impedances to reduce the work done by the user during repetitive tasks, or to off-load the user while stationary [13], [14]. A downside to passive wearables is that their impedance

This work has been funded by a grant from the Meta Reality Labs.

Alexander B. Ambrose is a PhD student in the Woodruff School of Mechanical Engineering, Georgia Institute of Technology, Atlanta, GA 30332, USA, alexander.ambrose@gatech.edu

Chelse VanAtter is an undergraduate student with the Department of Biomedical Engineering, Clemson University, Clemson, South Carolina 29634, USA, vanatte@g.clemson.edu

Frank L Hammond III is an Assistant Professor with the Woodruff School of Mechanical Engineering and the Coulter Department of Biomedical Engineering, Georgia Institute of Technology, Atlanta, GA 30332, USA, frank.hammond@me.gatech.edu

is usually fixed or cannot be easily adjusted on-demand.

On the other hand, robotic wearables can vary their impedance depending on the tasks users perform. Robotic wearables can be grouped into two categories, active and semi-active. Active wearables introduce energy to improve the performance of the individual. For example, during walking, active ankle prostheses may supply mechanical power to the ankle during the push-off phase of the gait cycle to lower the metabolic cost of transport for the individual [15]. Many active exoskeletons are intended for warfighters or the manual labor workforce to increase the load-carrying capability or to lower the metabolic cost of transport [16]–[18]. Semi-active wearables typically use impedance control to modify the stiffness, damping, and sometimes inertia of the device to increase the performance of the user during tasks [19]–[21]. This control strategy does not supply mechanical energy, but rather stores and releases or dissipates energy from the users.

For some applications, wearables need to have precise mechanical properties for the user to perform well. For example, a lower-limb prosthesis interface must accommodate loads during walking and other common tasks within a certain impedance range that is typically matched to a missing limb. If the impedance between the user and the prosthesis is not carefully controlled, users' could experience instability or decreased performance [22]. The impedance between a user and wearable end-effector is modulated by both the wearable's active or passive components, and by how well the wearable is fit to the user. Throughout the day and over longer periods, limb volume may change which impacts the fit of the socket [**?**], [23]. For example, if the limb volume shrinks, the impedance between the user and the prosthesis may decrease. Another more researched topic regarding wearable fit is to minimize areas of high pressure within the human-socket interface to decrease the risk of injury or skin damage [24].

The goal of the work presented here is twofold. The first goal is to design the semi-active wearable (SAW) that can simulate levels of fit, or in other words, achieve a specific impedance between the user and the end-effector. The second goal of this work is to validate that the SAW is behaving similar to an ideal linear impedance controlled two degree of freedom (DOF) manipulator. The SAW, shown in Fig. 1, is intended to be used in a human subject study to determine the effects of wearable device fit on users during an upper limb visuomotor tracking task. For this task, the participants will try to track a moving target on a screen with the laser-pointer end-effector of the SAW. This 2-DOF wearable device is capable of modifying both the linear stiffness and damping between the user and the laser-pointer end-effector using digital impedance control. The SAW has been validated by analyzing data from physical testing and simulation using MathWorks MATLAB and Simulink.

II. Design

The SAW is designed to simulate the various levels of fit of a forearm mounted wearable device by controlling the impedance between the user and the device's end-effector. Little research has been done to quantify the impedance of human-socket interfaces, especially in upper-extremity wearables. Therefore, the impedance for the SAW will mimic passive elbow, wrist, and finger impedance ranges [25]–[27]. The SAW is intended to be used in an upper-extremity visuomotor tracking task and is designed to be mounted on users' forearms. Rather than adjusting the impedance of the interface between the user and the wearable, the SAW simply changes the linear impedance between the user and the laser-pointer end-effector. To fully model the impedance between the user and a wearable end-effector, 6-DOF are needed, as shown in Fig. 2. However, to conserve weight to reduce the fatigue of users, the SAW was designed to have only two actuated DOF that correspond to the pitch and yaw of the end-effector. As the user accelerates the base of the wearable device, the joints of the SAW displace due to inertial torques. The coupled equations of motion (EOM) for both axes of the SAW were derived using the Iterative Newton-Euler Dynamic Formulations commonly used for manipulator dynamics following the process discussed in chapter 6 of *Introduction to Robotics: Mechanics and Control* [28]. The simplified model used to formulate the coupled EOM is shown in Fig. 3.

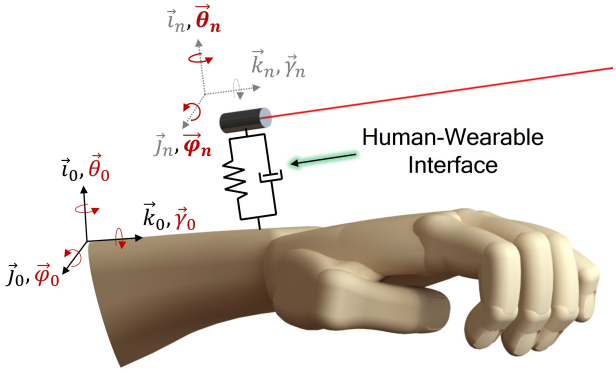

Fig. 2. Simplified diagram of a wearable with the goal to control the stiffness and damping between a user's forearm and the pitch (ϕ_n) and yaw (θ_n) rotations of the end-effector.

The EOM for this 2-DOF model are nonlinear similar to a

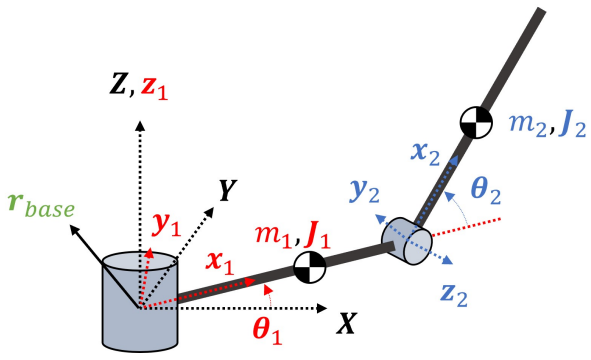

Fig. 3. Simplified Kinematic diagram of a 2-DOF wearable with r_{base} is the input to the system and θ_1 and θ_2 are the system outputs.

2-DOF pendulum model but with an added forcing function from base excitation and restoring torques due to control. This model assumes that joint friction is negligible. The first step in deriving the EOM is to determine the kinematics of the 2-DOF revolute manipulator. The angular velocity and acceleration of both links of the wearable device are determined using (1) and (2) respectively.

$$\boldsymbol{\omega}_i = \mathbf{R}_{\mathbf{i/i-1}}\boldsymbol{\omega}_{i-1} + \dot{\theta}_i\hat{\mathbf{z}}_i \tag{1}$$

$$\boldsymbol{\alpha}_i = \mathbf{R}_{\mathbf{i/i-1}}\boldsymbol{\alpha}_{i-1} + (\mathbf{R}_{\mathbf{i/i-1}}\boldsymbol{\omega}_{i-1} \times \dot{\theta}_i\hat{\mathbf{z}}_i) + \ddot{\theta}_i\hat{\mathbf{z}}_i \tag{2}$$

Here, i denotes the frame of the wearable device (1 or 2), $\mathbf{R}_{\mathbf{i/i-1}}$ is the rotation matrix from frame $i-1$ to the frame i, and $\hat{\mathbf{z}}_i$ is the unit vector for the rotation axis of link i. After the angular velocity and acceleration are determined the linear accelerations of the frames origin and center of mass (COM) of each link can be determined.

$$\begin{aligned}\mathbf{a}_i = \mathbf{R}_{i/i-1}(\boldsymbol{\alpha}_{i-1} \times \mathbf{r}_{i/i-1} + \\ \boldsymbol{\omega}_{i-1} \times (\boldsymbol{\omega}_{i-1} \times \mathbf{r}_{i/i-1}) + \mathbf{a}_{i-1})\end{aligned} \tag{3}$$

$$\mathbf{a}_{ci} = \boldsymbol{\alpha}_i \times \mathbf{r}_{ci/i} + \boldsymbol{\omega}_i \times (\boldsymbol{\omega}_i \times \mathbf{r}_{ci/i}) + \mathbf{a}_i \tag{4}$$

In (3) and (4), $\mathbf{r}_{ci/i}$ is the position of the COM of link i with respect to frame i. Once the linear and rotational kinematics have been determined, the kinetics of the manipulator can be determined.

$$\mathbf{F}_i = m_i\mathbf{a}_{ci} \tag{5}$$

$$\mathbf{N}_i = \mathbf{J}_{ci}\boldsymbol{\alpha}_i + \boldsymbol{\omega}_i \times \mathbf{J}_{ci}\boldsymbol{\omega}_i \tag{6}$$

Here, m_i and J_{ci} are the mass of the link i and the mass moment of inertia of link i taken at the COM and aligned with frame i. From here, the sum of the forces and torques acting on each link can be determined.

$$\mathbf{f}_i = \mathbf{R}^T_{i/i+1}\mathbf{f}_{i+1} + \mathbf{F}_i \tag{7}$$

$$\begin{aligned}\mathbf{n}_i = \mathbf{N}_i + \mathbf{R}_{i/i+1}\mathbf{n}_{i+1} + \mathbf{r}_{ci/i} \times \mathbf{F}_i + \\ \mathbf{r}_{i+1/i} \times \mathbf{R}_{i/i+1}\mathbf{f}_{i+1}\end{aligned} \tag{8}$$

Where, $\mathbf{R}_{i/i+1}$ is the rotation matrix from $i+1$ to i and $\mathbf{r}_{i+1/i}$ is the position of frame $i+1$ with respect to frame i. To determine the joint torques at each joint the following equation is used.

$$\tau_i = \mathbf{n}_i \cdot \hat{\mathbf{z}}_i \tag{9}$$

Using impedance control, where the joint torque is proportional to the joint position and joint velocity, the closed form EOM can be derived.

$$\tau_i + C_i\dot{\theta}_i + K_i\theta_i = 0 \tag{10}$$

Here, C_i and K_i are the damping coefficient and the stiffness of each link. For a 2-DOF manipulator, a set of two coupled EOM, $i = 1$ and $i = 2$, will be solved together.

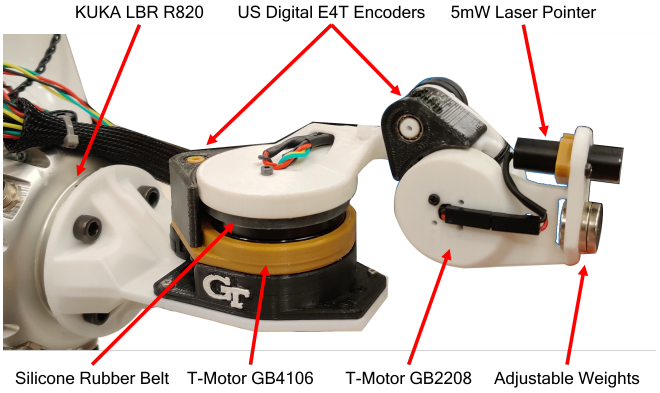

Fig. 4. Labeled picture of the motorized SAW mounted on the KUKA LBR iiwa 14 R820 for 2-DOF base excitation.

A. The Semi-Active Wearable

The SAW, as shown in Fig. 4, was designed to utilize two motorized revolute joints that each mimic a linear torsional spring and damper. The SAW uses two brushless direct-current (BLDC) gimbal motors from T-Motor (GB2208 for the pitch axis and GB4106 for the yaw axis). Gimbal motors were chosen for this robotic application due to their benefits over other BLDC motors. Gimbal motors have orders of magnitude higher phase resistance than other BLDC motor types. The high phase resistance of gimbal motors reduces power consumption. Furthermore, these gimbal motors have speed constants of 506 and 1,222 RPM/V for the GB4106 and GB2208 respectively. The relatively low-speed constants and an out-runner design mean their torque density is higher than other BLDC motor types of the same form factor [29]. Since the weight of the SAW was to be minimized, a high torque density direct-drive actuator was needed.

The two motors on the SAW are coupled with silicone rubber belts to US Digital E4T incremental encoders with 360 counts per revolution (CPR). The benefit of coupling the encoder to the motor using a belt is that the gear ratio between the motor and the encoder is increased, theoretically increasing the angular precision of the actuator. The silicone belts were made from Smooth-Sil 960 silicone rubber and were pre-tensioned by under-sizing the belts by 25%. Pre-tensioning the silicone rubber belts increases the stiffness of the belts in the hopes of not disrupting the commutation of the motors. A belt with high stiffness is more favorable, than one with low stiffness, however, it was found that under-sizing the belts more than 25% severely reduced the longevity of the belts. The encoder shafts are supported by two 0.25 in internal diameter radial ball bearings. These ball bearings were chosen over bushings to minimize the friction of the encoder shafts. The friction of the encoder shafts also would cause the belts to stretch, disrupting commutation and motor feedback.

An ODrive 24 Volt motor controller was used to control the torque these two gimbal motors produced. For the impedance controller, a Texas Instruments MSP432 micro-controller was used to communicate with the ODrive motor controller using UART serial communication with a baud rate

of 460800 bps. The microcontroller's role was to calculate and prescribe the motor torques based on the angular position feedback from both encoders. The microcontroller receives motor controller feedback and commands each axis of the SAW at 200 Hz. After performing a simulation of the 2-DOF system, it was found that a control frequency of 200 Hz provided stable operation for excitation frequencies less than 2 Hz. The torque controller of the ODrive was tuned to have a bandwidth of 1 kHz to ensure that the current control PI loop is not adding significant latency to the controller. The calculation used to determine the necessary motor current to produce the correct torque is shown in (11).

$$I = \frac{K}{K_\tau}\theta + \frac{C}{K_\tau}\dot{\theta} \tag{11}$$

The velocities of the motors were approximated using a two-point backward finite difference since the velocity estimation from the ODrive motor controller was found to be inaccurate at speeds less than 10 revolutions per minute.

$$\dot{\theta} \approx \frac{1}{T}(\theta[k] - \theta[k-1]) \tag{12}$$

Here, *k* is the current time step and *T* is the sampling time of 5 milliseconds. For this method, a single previous angular position needs to be stored.

Since the motors selected for this use case are gimbal motors with phase resistances of 7.2 Ω for the GB2208 and 7.65 Ω for the GB4106, the ODrive motor controller had to use voltage control to estimate and control the current that is running through the motors via Ohm's law. This relatively high phase resistance means that the maximum current going through the motors is less than 4 Amps for each motor, which is too low for the current sensors on the ODrive motor controller to precisely measure, hence, voltage control is implemented rather than the traditional current control method. It is thought that this estimation assumes that the motor velocities are small enough that the back EMF from the motors is negligible.

$$I = \frac{V_{motor} - V_{EMF}}{R_{motor}} \approx \frac{V_{motor}}{R_{motor}} \tag{13}$$

The error in the current approximation in (13) is dependent on the applied voltage and the speed of the motors. For high torque and low-speed applications, this approximation tends to be accurate. But, for high-speed and low torque applications, this approximation will not be accurate.

Possibly due to the stretchable belt coupling the motors to the encoders, the motors would tend to vibrate about the equilibrium point. If damping coefficients were set above 5 mNms/rad, the vibrations would become unstable and grow in amplitude. To fix this issue, a 20-point running average filter was used on the positions used to approximate the velocities. This allowed higher damping coefficients to be utilized. However, this filter does introduce a delay in the damping control of the SAW.

B. Simulating the SAW

Simulation of the SAW was conducted using MathWorks Simscape. The Simscape Multibody Link plugin was used to convert a simplified SolidWorks assembly of the robotic device into a Simscape model autonomously. The Simscape Multibody Link plugin also carries the mass and inertia properties from the SolidWorks assembly. This assembly of the SAW is simplified by letting the entire mass of each motor spin with the output of the motor. Each motor was weighed and the masses of the motors in the simulation were overwritten with the measured mass of the motors. The simulation also assumes that the device is frictionless and the weight of the assembly hardware and wires do not significantly affect the mechanics of the device. The joints of the model were modified to be controlled by torque signals and produce displacement feedback signals. The simulated impedance controller sampled the joint positions and produced torque signals at the same rate as the real device, 200 Hz per axis. The joint velocities were again approximated using a two-point backward difference. The commanded torque to each joint was calculated by multiplying the right hand side of (11) by the measured torque constants of the motors. The commanded torques were bounded by the approximated stall torque of the motors which was calculated via the following approximation since the stall torque of this motor was not disseminated by the manufacturer.

$$\tau_{stall} \approx \frac{K_\tau V_{max}}{R_{phase}} \tag{14}$$

Here, the maximum applied voltage to the motors measured in Volts is V_{max}, the phase resistance measured in Ohms is R_{phase}, and the measured torque constants of the motors in Nm/A is K_τ. Using (14), the theoretical stall torque for the GB2208 and GB4106 are 21 and 46 mNm respectively while operating at a max voltage of 20 Volts.

The mass moment of inertia of the links of the SAW are what induce the axes to deflect away from equilibrium as the user accelerates the base of the device. In order for both axes of the SAW to have the same damped natural frequency, the stiffnesses and damping coefficients of both axes of the SAW must be different from one another. The ratio between the links' stiffness and damping coefficients was found through iterative simulations where the base of the SAW was excited in 2 dimensions. After this calibration simulation, a non iterative version of this simulation was used to validate the SAW by comparing the measured joint displacements of the SAW during 2-dimensional base excitation.

III. Experiment Design

The motors of the SAW were tested using a KUKA LBR iiwa 14 R820 manipulator with an ATI mini 45 force/torque sensor attach to its end-effector.

A. 1-DOF Testing

For these tests, the motor outputs were coupled to the ATI sensor directly using 3D printed components and the base of the motors was clamped to a large table. The motors were commanded to draw 1 Amp and the resulting torques were measured. A total of five trials were recorded for each motor and the measured torque produced was averaged to

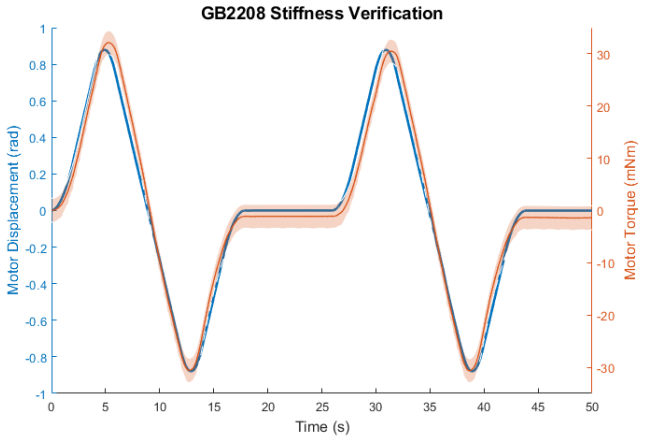

Fig. 5. An example of the prescribed KUKA end-effector rotation to induce the motor displacement and the measured torque produced by the GB2208 motor. The torque presented here is the difference between the average measured torque with a stiffness of 30 mNm/rad and the average measured torque for the three control trials. The orange highlighted region shows the standard deviation of the measured torque.

determine the torque constants for each motor. Once the torque constants of the motors were verified, the impedance controller was tested. The stiffness and damping of the impedance controller were first evaluated individually. To test the stiffness the motors simulated, the damping coefficients in the impedance controller were set to zero. To test the damping the motors simulated, stiffness was set to zero in the impedance controller. For the stiffness tests, the KUKA was used to rotate the outputs of the motors at constant velocity using trapezoidal velocity trajectories with a displacement amplitude of 1 rad. The angular displacements and the torque generated by the motors were recorded at 200 Hz. To test the damping of the impedance controller, the KUKA was used to rotate the outputs of the motors again using trapezoidal velocity trajectories. However, this time the KUKA rotated the motors with increasing rates of displacements so the torque produced by the motors could be correlated with the speed of the motor output.

Three control trials were first performed with the motors commanded to output 0 Nm for the duration of the trial for both the stiffness and damping trajectories. These control trials were used to measure the torsional friction of the actuator. After these three control trials, both motors were commanded to behave like linear springs and dampers with stiffnesses of 30 mNm/rad and damping coefficients of 20 mNms/rad. Five trials were performed for each motor and for both the stiffness and damping verification tests. The average measured torques as a function of time for the control trials were subtracted from the measured torque time series from the five trials where the motors behaved like springs and dampers, yielding corrected measured torque time series. Examples of the KUKA end-effector trajectories and the corrected measured torques for both the stiffness and damping verification are shown in Fig. 5 and Fig. 6.

B. 2-Dimensional Base Excitation

After ensuring that the motors were performing like linear torsional springs and dampers, both degrees of freedom of the SAW were tested simultaneously. For this test, the base of the SAW was attached to the KUKA end-effector as shown in Fig. 4 and each joint was commanded to behave like a spring and damper simultaneously. The KUKA was commanded to move the base of the SAW in a circle in a plane parallel to the y-z plane as shown in Fig. 7. This circular motion was accomplished by commanding the 3rd and 4th joints of the KUKA to displace harmonically at a frequency of 1 Hz. This motion was chosen to try to replicate the motion an individual would use while trying to track a moving target with the end-effector of the SAW using medial-lateral shoulder rotation coupled with flexion-extension of the elbow. The rotation of the orientation vector of the end-effector was assumed to yield negligible effects on the SAW and was disregarded for the simulation of the SAW. The displacements of the joints of the SAW were recorded at 200 Hz during this test and compared to the joint displacements in simulation.

To generate the 2-dimensional base excitation, the KUKA was commanded to go through 300 Cartesian waypoints that approximate a circle with a radius of 5 cm in a plane parallel to the y-z plane of the manipulator. To avoid large KUKA accelerations at the beginning and end of this trajectory, the joint velocities of the KUKA were modulated from zero to the initial starting velocities and again from the final joint velocities back to zero. These velocity ramping phases of the circle trajectory took one circular period over 2.25 seconds. The 3rd and 4th steady-state joint trajectories in radians used to create this circular motion are shown in (15) and (16).

$$q3(t) = 0.1cos(\omega t - \pi/2) \tag{15}$$

$$q4(t) = 0.1sin(\omega t - \pi/2) - \pi/2 \tag{16}$$

The control frequency of the KUKA manipulator was 600 Hz. Fig. 7 shows the orientation and trajectory of the KUKA end-effector. Five trials were performed with the KUKA

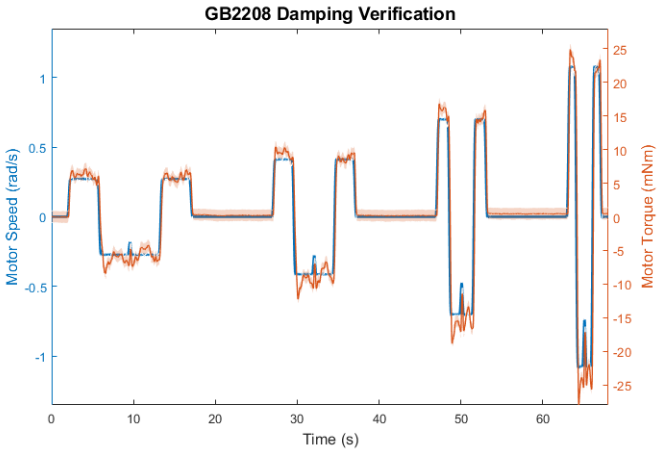

Fig. 6. An example of the prescribed KUKA end-effector rotational velocity to induce the motor displacement and the measured torque produced by the GB2208 motor. The torque presented here is the difference between the average measured torque with a damping coefficient of 20 mNms/rad and the average measured torque for the three control trials. The orange highlighted region shows the standard deviation of the measured torque.

exciting the base of the SAW. Before each trial, the motors were recalibrated and zeroed.

C. 2-DOF Simulation

In the simulation, the base of the SAW was displaced according to the 2-dimensional Cartesian curves calculated using forward kinematics from the average measured KUKA joint positions from physically testing the trajectories implemented on the KUKA. First, iterative simulations were conducted to find the ratios between both joints' stiffnesses and damping coefficients that would yield the same damped natural frequencies for both axes. After achieving the correct ratio between the two joints' stiffnesses and damping coefficients, the SAW was tested again with the stiffnesses and damping coefficients obtained from the iterative simulations. Five trials were performed on the KUKA and the average joint displacements of the SAW were compared to the joint displacements from a single simulation.

IV. Results and Discussion

A. Torque Constant Testing

The measured torque constants for the GB2208 and GB4106 are shown in table I. After measuring the torque constants of both motors, they were verified by performing the same tests with the measured torque constants updated in the motor controller. Instead of commanding 1 A of motor current, both motors were commanded to output 30mNm and the torque they produced was measured. The GB2208 output an average torque of 29.8 $\pm$ 2.0 mNm and the GB4106 output an average torque of 31.3 $\pm$ 1.7 mNm. The measured torque produced by both motors was within one standard deviation of the prescribed torque.

B. Impedance Control Verification

For the impedance verification, the stiffness and damping of the motors were tested individually. For the stiffness verification, the damping ratio in the controller was set to zero and for the damping verification, the stiffness parameter was set to zero. To determine the stiffness the motors were simulating, the measured torque time series was plotted against the motor position time series. A linear polynomial fit was then used to determine the correlation between motor position and the output torque of the motor, yielding the equivalent stiffness of the motors. Similarly, for the damping verification, the measured torque time series was plotted against the motor velocity, and the data was again fitted with a linear fit. Examples of the time series of measured torque, motor displacement, and motor velocity have already been shown in Fig. 5 and Fig. 6. The results of the stiffness and damping verification are shown in Table II. Again, the prescribed stiffness and damping coefficients for both motors were 30 mNm/rad and 20 mNm/rad respectively.

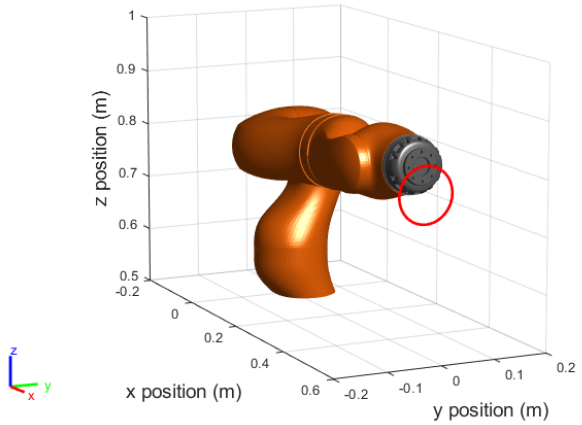

Fig. 7. Rendering of the end-effector of the KUKA LBR iiwa 14 R820 and the Cartesian trajectory used to perform harmonic base excitation of the SAW for simulation and physical testing.

TABLE I
MEASURED TORQUE CONSTANTS

Motor	Measured K_τ (mNm/A)
GB2208	7.59 $\pm$ 0.27
GB4106	17.6 $\pm$ 1.6

TABLE II
MEASURED STIFFNESS AND DAMPING COEFFICIENTS

Motor	Measured K (mNm/rad)	Measured C (mNms/rad)
GB2208	31.9 $\pm$ 2.3	21.8 $\pm$ 0.9
GB4106	32.3 $\pm$ 3.0	20.8 $\pm$ 1.2

C. 2-Dimensional Base Excitation Simulations

To determine the stiffness and damping coefficients of each link of the wearable device that would yield similar damped frequencies for both axes and iterative simulation solver was constructed. The simulated amplitudes of the joint displacements and the phase delay between the base excitation and the joint motion were observed. The ratio of the two joint displacement amplitudes and phase delays was created to help determine the correct stiffness and damping ratios between the two joints. After every simulation iteration, the first joint parameters were adjusted depending on the ratios between joint displacement amplitudes or the ratio of the phase delays. The stiffness and the damping of the second joint were selected as 1 mNm/rad and 1 mNms/rad, while the first joint properties were changed after every iteration of the simulation. The simulation was run with an initial joint stiffness and damping of 10 mNm/rad and 10 mNms/rad for the first link. The amplitude of the displacements of both joints and the phase delay of both joints were collected. The first joint stiffness was then divided by the ratio of the joint displacement amplitudes and the simulation was run again. This stiffness adjustment was repeated until the amplitude of displacements for both joints was observed to be within 1% of one another. Once the amplitudes of both joint displacements were within 1% of one another, the first joint's damping was divided by the ratio of phase delays, and the simulation was run again. The damping coefficient of the first joint was adjusted until the phase delays of the two joints were within 1% of one another. Then the whole process repeats until both the amplitudes and the phase delays of the

two joints were simultaneously within 1% of one another.

The joint stiffness and damping coefficients for the first joint converged to 12.7 mNm/rad and 11.1 mNms/rad. These stiffness and damping coefficients for both links were updated in the impedance controller for the SAW and physical base excitation was performed.

D. 2-Dimensional Base Excitation

To further validate the impedance controller, the fully assembled SAW was tested. The base of the SAW was mounted on the KUKA manipulator, shown in Fig. 4, which performed the base excitation. The measured joint positions of the SAW were compared to simulated joint positions. The joint positions of the SAW and simulation are shown in Fig. 8. The simulated and measured joint displacement time series were synced together by finding the time where the velocities of the joints were measured to be greater than zero. It is thought that the discrepancies between the simulated joint displacements and the measured joint displacements are due to the simplification of the simulation. Firstly, the simulation assumes that the SAW is frictionless. Secondly, the mass and the inertia of the SAW links are greater than the simulated wearable device. This increased mass and inertia are evident since the measured peak-to-peak displacements of the SAW are greater than the simulated response. The test data shows periodic plateaus after the peaks in displacement. These plateaus are thought to come from the filter used in estimating the joint velocity and/or the presence of friction. The filter adds a delay of about 0.1 seconds in the impedance controller which may be why these plateaus occur approximately 0.1 seconds after the joint velocities change sign.

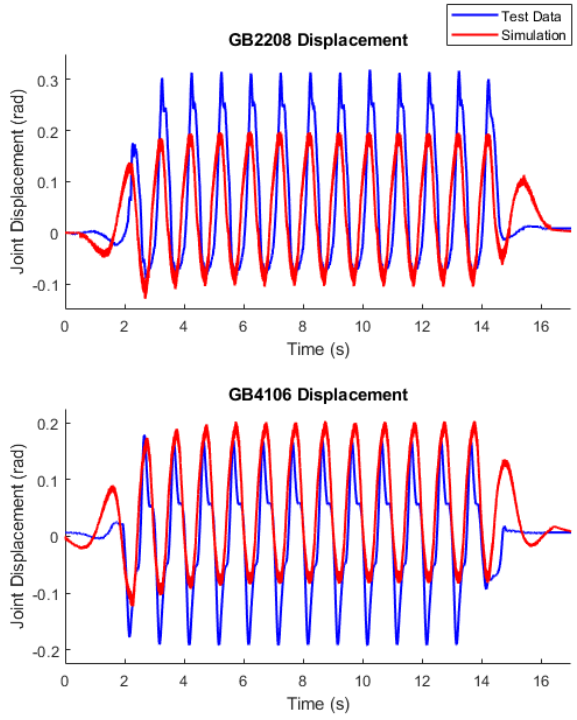

Fig. 8. Measured joint displacements (blue) and simulated joint displacements (red) as a function of time while undergoing circular harmonic base excitation with a radius of 5 cm and a frequency of 1 Hz. The stiffness and damping coefficients used for the simulation and physical tests were found from the previous simulation that yielded the ratios of stiffnesses and damping coefficients that produce the same damped natural frequencies of both links of the SAW.

V. Conclusion

There is little research investigating the impact of wearable device fit on users' task performance and cognitive load. Current research into the human-socket interface of wearables focuses on reducing the average pressure imparted on the individuals limb to improve comfort and reduce the risk of injury and medical issues. The semi-active wearable presented here is being used in a concurrent study to simulate varying levels of transradial wearable device fit. This work will focus on how impedance between a user and a wearable or prosthesis end-effector will affect the users ability to perform dynamic tracking tasks. The semi-active wearable presented here has been verified by showing that the device can control the linear stiffness and damping between the base and end-effector of the device in 2 axes. The work presented here has shown that each axis of the SAW behaves similarly to the derived 2-DOF model and simulated model.

In the future, the discrepancies between the 2-DOF model and the SAW will be decreased by increasing the control frequency of the impedance controller to overcome the instability issues as the prescribed damping coefficients are increased. This increased control frequency will also facilitate the removal of the filter used to estimate the joint velocities of the SAW, which is thought to add plateaus to the 2-DOF base excitation response. The SAW also has limitations, such as only approximating linear stiffness and damping. The impedance of common human-wearable interfaces is not known, but the control of this wearable device could be adjusted to a nonlinear impedance simply by changing the impedance control algorithm. Another limitation is the lack of active gravity compensation. It is assumed that the user will be positioning the SAW in the upright orientation, and only a passive torque offset is used on the pitch axis to compensate for the torque imparted on the joints due to gravity. If the user were to rotate their forearm in supination-pronation, the joints of the SAW would displace away from equilibrium. For this reason, inertial measurement units will be implemented to institute active gravity compensation. Furthermore, a passive adjustment strap is used to secure the wearable device to users' forearms. In future work, these inertial measurement units will be placed on the forearm of the user and the base of the wearable device to ascertain the displacements between users and the base of the SAW in real-time. This displacement measurement will be used as an input into the control algorithm so that the impedance between users' forearms and the end-effector of the SAW can be consistent across all users. Once these modifications are made, the SAW will be used to simulate varying levels of fit of a forearm wearable device to assess how the level of fit can affect a user performing a visuomotor tracking task.

ACKNOWLEDGMENT

The authors would like to thank Dr. Yigit Menguc and Dr. Tanya Jonker at Meta Reality Labs for their insights and direction on this project.

REFERENCES

[1] M. Cempini, S. M. M. De Rossi, T. Lenzi, M. Cortese, F. Giovacchini, N. Vitiello, and M. C. Carrozza, "Kinematics and design of a portable and wearable exoskeleton for hand rehabilitation," *2013 IEEE 13th International Conference on Rehabilitation Robotics (ICORR)*, pp. 1–6, 2013.

[2] J. Liu *et al.*, "Kinematics study of a 10 degrees-of-freedom lower extremity exoskeleton for crutch-less walking rehabilitation," *Technology and health care : official journal of the European Society for Engineering and Medicine*, 2021.

[3] "Development and measurement properties of the orthotics and prosthetics users' survey (opus): A comprehensive set of clinical outcome instruments," *Prosthetics and Orthotics International*, vol. 27, pp. 191–206, 2003.

[4] L. Demers, R. Weiss-Lambrou, and B. Ska, "Item analysis of the quebec user evaluation of satisfaction with assistive technology (quest)," *Assistive Technology*, vol. 12, pp. 96–105, 2000.

[5] M. R. Safari and M. R. Meier, "Systematic review of effects of current transtibial prosthetic socket designs-part 2: Quantitative analysis," *Journal of Rehabilitation Research Development*, vol. 52, pp. 509–526, 2015.

[6] B. J. Darter, K. Sinitski, and J. M. Wilken, "Axial bone - socket displacement for persons with traumatic transtibial amputation: The effect of elevated vacuum suspension at progressive body-weight loads," *Prosthetics and Orthotics International*, vol. 40, pp. 552–557, 2014.

[7] H. Lee, E. J. Rouse, and H. I. Krebs, "Summary of human ankle mechanical impedance during walking," *IEEE J Transl Eng Health Med*, vol. 4, p. 2100407, 2016.

[8] E. J. Rouse, L. J. Hargrove, E. J. Perreault, and T. A. Kuiken, "Estimation of human ankle impedance during the stance phase of walking," *IEEE Trans Neural Syst Rehabil Eng*, vol. 22, no. 4, pp. 870–8, 2014.

[9] W. Hoogkamer, S. Kipp, J. H. Frank, E. M. Farina, G. Luo, and R. Kram, "A comparison of the energetic cost of running in marathon racing shoes," *Sports Med*, vol. 48, no. 4, pp. 1009–1019, 2018.

[10] K. A. Boyer, P. Federolf, C. Lin, B. M. Nigg, and T. P. Andriacchi, "Kinematic adaptations to a variable stiffness shoe: mechanisms for reducing joint loading," *J Biomech*, vol. 45, no. 9, pp. 1619–24, 2012.

[11] R. Nagahara, H. Kanehisa, and T. Fukunaga, "Influence of shoe sole bending stiffness on sprinting performance," *J Sports Med Phys Fitness*, vol. 58, no. 12, pp. 1735–1740, 2018.

[12] H. W. van Jaarsveld, H. J. Grootenboer, J. de Vries, and H. F. Koopman, "Stiffness and hysteresis properties of some prosthetic feet," *Prosthet Orthot Int*, vol. 14, no. 3, pp. 117–24, 1990.

[13] M. S. Cherry, S. Kota, A. Young, and D. P. Ferris, "Running with an elastic lower limb exoskeleton," *J Appl Biomech*, vol. 32, no. 3, pp. 269–77, 2016.

[14] K. Huysamen, T. Bosch, M. de Looze, K. S. Stadler, E. Graf, and L. W. O'Sullivan, "Evaluation of a passive exoskeleton for static upper limb activities," *Appl Ergon*, vol. 70, pp. 148–155, 2018.

[15] S. K. Au, H. Herr, J. Weber, and E. C. Martinez-Villalpando, "Powered ankle-foot prosthesis for the improvement of amputee ambulation," *Annu Int Conf IEEE Eng Med Biol Soc*, vol. 2007, pp. 3020–6, 2007.

[16] A. J. E. Bequette, B. Norton and L. Stirling, "The effect of a powered lower-body exoskeleton on physical and cognitive warfighter performance," *Proceedings of the Human Factors and Ergonomics Society Annual Meeting*, vol. 62, no. 1, pp. 1663–1667, 2018.

[17] L. M. Mooney, E. J. Rouse, and H. M. Herr, "Autonomous exoskeleton reduces metabolic cost of human walking during load carriage," *J Neuroeng Rehabil*, vol. 11, p. 80, 2014.

[18] G. E. P. M. A. Aguirre-Ollinger, G. Colgate and A. Goswami, "Active-impedance control of a lower-limb assistive exoskeleton," *2007 IEEE 10th International Conference on Rehabilitation Robotics*, pp. 188–195, 2007.

[19] A. Blank, AA. Okamura and W. LL., "Task-dependent impedance and implications for upper-limb prosthesis control," *The International Journal of Robotics Research*, vol. 33, no. 6, pp. 827–846, 2014.

[20] B. E. Lawson and M. Goldfarb, "Impedance admittance-based coordination control strategies for robotic lower limb prostheses," *ASME. Mechanical Engineering*, vol. 136, no. 9, pp. S12–S17, 2014.

[21] N. Hogan, "Impedance control: An approach to manipulation," *1984 American Control Conference*, pp. 304–313, 1984.

[22] E. Isakov *et al.*, "Standing sway and weight-bearing distribution in people with below-knee amputations," *Archives of Physical Medicine and Rehabilitation*, vol. 73, no. 2, pp. 174–178, 1992.

[23] L. L. D. L. H. Perreault, E. Hargrove and J. Sensinger, "Considering limb impedance in the design and control of prosthetic devices," *Artemiadis P. (eds) Neuro-Robotics: Trends in Augmentation of Human Performance*, vol. 2, pp. 188–195, 2014.

[24] D. M. Sengeh and H. Herr, "A variable-impedance prosthetic socket for a transtibial amputee designed from magnetic resonance imaging data," *Journal of Prosthetics and Orthotics*, vol. 25, pp. 129–137, 2013.

[25] S. Durand, C. P. Rohan, T. Hamilton, W. Skalli, and H. I. Krebs, "Passive wrist stiffness: The influence of handedness," *IEEE Trans Biomed Eng*, vol. 66, no. 3, pp. 656–665, 2019.

[26] P. H. Kuo and A. D. Deshpande, "Muscle-tendon units provide limited contributions to the passive stiffness of the index finger metacarpophalangeal joint," *J Biomech*, vol. 45, no. 15, pp. 2531–8, 2012.

[27] C. E. Lang and M. H. Schieber, "Human finger independence: limitations due to passive mechanical coupling versus active neuromuscular control," *J Neurophysiol*, vol. 92, no. 5, pp. 2802–10, 2004.

[28] J. Craig, *Introduction to Robotics Mechanics and Control*, ser. Fourth Edition. Pearson Education, 2018.

[29] S. D. Sensinger, J.W. Clark and J. F. Schorsch, "Exterior vs. interior rotors in robotic brushless motors," in *2011 IEEE International Conference on Robotics and Automation*, 2011, pp. 2764–2770.